Journal of
Ceramic Science
and Technology

J. Ceram. Sci. Technol., **17** [3] 237-254 (2026)
DOI: 10.4416/JCST2026-00007
available online at: http://www.ceramic-science.com
© 2026 Göller Verlag

Research on Highly Sensitive Amorphous Silicon-Carbon Nanocomposite Strain Sensors for Motion Capture

Bing Liang*, Tingna Zhou, Ling Zeng

College of Physical Education, Hunan International Economics University, Changsha, 430205, China
received April 22, 2026; received in revised form July 14, 2026; accepted August 17, 2026

Abstract

Amorphous silicon-carbon nanocomposite strain sensors are promising for wearable motion capture because they can combine chemically tunable mixed-bond networks with mechanically compliant conductive pathways. In this work, four flexible sensor groups, denoted S1 – S4, were fabricated by varying carbon enrichment and network-conversion intensity in precursor-derived amorphous silicon-carbon sensing layers. Comparative characterization showed that all active layers remained predominantly amorphous while exhibiting progressive changes in carbon-domain disorder, Si-C related bonding fraction, nanoscale conductive-domain size, surface roughness, and crack-prone mesoscale texture. Among the four samples, S3 showed the most favorable chemical-state window, with the highest Si-C related bond fraction, the most favorable surface roughness, and the best balance between conductive continuity and reversible pathway instability. This structural combination was associated with superior electromechanical performance, including gauge factors of 17.4 at 0 – 10 % strain, 73.8 at 10 – 40 % strain, and 286.7 at 40 – 80 % strain, a working range of 0 – 90 %, a minimum detectable strain of 0.10 %, a response time of 81 ms, and 93.3 % signal retention after 10 000 cycles. The optimized device also maintained good stability under humidity and temperature variations, storage, and repeated bending and monitored finger, wrist, elbow, knee, throat, and facial-expression motion. The results suggest that high-performance motion capture in this material system is governed not by maximum carbonization alone, but by a balanced amorphous silicon-carbon network that couples moderate roughness, interfacial anchoring, and reversible crack-mediated conductive-path modulation.

Keywords: Amorphous silicon-carbon, strain sensor, motion capture, wearable electronics, nanocomposite

I. Introduction

Flexible strain sensors have become essential components in emerging wearable electronics because they can transduce subtle mechanical deformation into measurable electrical signals for motion recognition, soft robotic feedback, and non-invasive human-machine interaction [1–3]. In recent years, the field has shifted from simple proof-of-concept devices toward multifunctional sensing platforms capable of resolving both large-amplitude joint motion and weak biomechanical deformation with acceptable repeatability, low hysteresis, and high environmental tolerance. This shift has exposed a persistent materials problem. Many highly stretchable sensors deliver only moderate sensitivity, while highly sensitive crack-based or percolation-dominated devices often suffer from limited linear range, unstable baselines, or poor long-term durability. Carbon nanotube fiber sensors, for example, can sustain very large deformation and remain suitable for wearable monitoring, yet their performance envelope illustrates the broader challenge of balancing stretchability with stable signal amplification under repeated use [4]. Likewise, thread-based and polymer-composite resistive sensors have demonstrated practical motion-monitoring capability, but their reported gauge factors, working windows, and frequency stability still reveal pronounced tradeoffs between sensitivity, range, and robustness [5,6].

A major direction in the field has therefore been the structural engineering of conductive networks. Instead of relying only on filler loading, recent studies have shown that wrinkle formation, crack regulation, hierarchical bridging, and microtexture design can strongly amplify strain-induced resistance modulation. Crack-assisted systems can reach extremely high gauge factors at large deformation, but the same structural features that produce intense signal amplification can also introduce nonlinearity, irreversible path disruption, or high dependence on the exact crack geometry [1]. Other reports have attempted to mitigate this problem by constructing wrinkled, bridged, or layered conductive networks so that the electrical pathway can be disrupted progressively rather than catastrophically during stretching [7,8]. These approaches demonstrate that sensor performance is governed not merely by conductivity itself, but by the way conductive pathways evolve under mechanical loading. In practical terms, the most useful wearable strain sensor is rarely the one with the single largest gauge factor; it is the one that preserves an advantageous compromise

* Corresponding author: swim_lb@126.com

between low-strain resolution, medium-strain linearity, high-strain responsiveness, response speed, and cycle-to-cycle reproducibility [2,9].

Although carbon-rich composites dominate the current landscape, silicon-containing amorphous networks offer a less explored but potentially valuable design space. Amorphous silicon-carbon systems can accommodate mixed Si-C, C-C, and silicon-oxygen-carbon local environments, and this bonding diversity may be exploited to tune short-range order, interfacial adhesion, and strain-dependent conductive path reconstruction. Prior work on amorphous Si-C films has shown that silicon incorporation and processing conditions can substantially alter Raman disorder parameters, local bonding signatures, and nanoscale surface characteristics [10]. Related studies on silicon oxycarbide thin films have further demonstrated that amorphous silicon-carbon-oxygen networks exhibit identifiable Si-C and Si-O-Si signatures in Fourier transform infrared spectroscopy (FTIR) and X-ray photoelectron spectroscopy (XPS) while maintaining uniform thin-film morphology and chemically heterogeneous local structures [11]. These observations are significant for flexible sensing because resistive strain transduction in amorphous conductive media depends strongly on the coexistence of conductive carbon domains, mechanically compliant matrix regions, and interfacial sites that regulate crack initiation and tunneling distance during deformation. However, despite the mature literature on carbon nanotube, graphene, carbon black, and hybrid metallic-polymer sensors, reports directly exploiting silicon-containing carbonaceous networks for wearable strain sensing remain comparatively scarce. Even among recent examples, silicon-related flexible sensors are still often built around silicon carbide or mixed carbon allotrope architectures rather than systematically tuned amorphous silicon-carbon nanocomposites [12].

This gap suggests that amorphous silicon-carbon nanocomposites merit investigation not as a trivial variation of conventional carbon-filled elastomers, but as a platform in which chemical-state regulation, roughness evolution, and crack-mediated conductive reconfiguration can be co-designed. A comparative multi-sample study is particularly necessary because single-sample optimization cannot reveal whether improved response originates from enhanced pathway continuity, controlled disorder, increased roughness, or simply from excessive carbon enrichment. If conductivity rises monotonically while sensing quality does not, then the relevant design principle is not maximum carbonization but balanced network engineering. For wearable motion capture, that balance should ideally produce a sensor capable of resolving weak deformation at low strain, preserving linear and repeatable responses through moderate strain, and retaining a distinct signal at large strain without severe hysteresis drift.

Accordingly, this work investigates four amorphous silicon-carbon nanocomposite strain sensors with systematically tuned network structures and compares their structural, chemical, topographic, mechanical, and electromechanical characteristics. The study is designed around three hypotheses. First, increasing carbon enrichment and Si-C related bonding should improve pathway continuity up to an optimum point. Second, moderate roughness and controlled microcrack evolution should amplify resistance modulation more effectively than either an overly smooth or an over-stabilized surface. Third, the best overall motion-capture performance should emerge from a network that balances conductivity, deformability, and reversible path reconstruction rather than maximizing any single parameter in isolation.

II. Materials and Methods

The amorphous silicon-carbon nanocomposite sensing layers were designed as carbon-enriched silicon-containing conductive films integrated onto flexible elastomeric substrates. A silane-derived preceramic precursor was used as the silicon source, while a carbon-forming additive and a dispersed nanocarbon phase regulated the formation of carbonaceous conductive domains after thermal conversion. The precursor solution was prepared by sequentially mixing the silicon-containing oligomer, ethanol, deionized water, and acid catalyst to initiate partial hydrolysis and condensation. After magnetic stirring for 2 h at room temperature, the carbon-forming additive and nanoscale carbon dispersion were introduced and further homogenized by means of combined stirring and ultrasonication. The resulting suspension was aged for 12 h to stabilize viscosity before film deposition.

Four sample groups, denoted S1, S2, S3, and S4, were fabricated by varying the relative carbon enrichment and the conversion intensity of the precursor-derived network. S1 was produced with the lowest carbon fraction and the mildest thermal conversion condition, yielding a relatively discontinuous conductive network. S2 employed a higher carbon-loading level and slightly stronger conversion to improve conductive continuity. S3 was prepared under the optimized condition in which the carbonized domains, Si-C related bonding fraction, and surface roughness jointly promoted strain-sensitive pathway modulation. S4 used the highest carbon-enrichment level and the strongest conversion condition so that its baseline conductivity exceeded that of the other samples, although excessive network stabilization was expected to reduce strain-amplified resistance change at larger deformation. In all cases, the precursor films were deposited onto pre-cleaned polydimethylsiloxane substrates by doctor-blade coating with a fixed coating gap, followed by solvent evaporation at 60 °C for 1 h and stepwise thermal treatment under argon. The conversion temperature was maintained below the range required for bulk crystallization so that the resulting sensing layer retained its amorphous character while developing carbon-rich conductive domains.

After thermal conversion, the films were patterned into rectangular sensing elements with an effective gauge length of 20 mm and an active width of 5 mm. Stretchable silver-paste electrodes were applied at both ends of the active region and reinforced with copper leads

for electrical connection. A thin protective elastomer overlayer was laminated along the electrode-transition region to reduce interfacial delamination during repeated loading while leaving the sensing region itself exposed for mechanical transduction. The effective gauge length was defined as the exposed sensing-layer distance between the inner electrode edges; the protective overlayer and electrode-transition region were not included in the gauge length used for resistance-strain calculations. Film thickness was reported from the cross-sectional/geometric measurement set summarized in **Fig. 1e** and **Table 1**, and active length and width were checked from the patterned sensing area before electrode reinforcement. The macroscopic appearance and geometric configuration of the fabricated devices are presented in **Fig. 1**, where **Fig. 1a** shows the S1 – S4 devices, **Fig. 1b** demonstrates the flat, bent, and stretched states, **Fig. 1c** enlarges the electrode-transition region, **Fig. 1d** presents the cross-sectional architecture, and **Fig. 1e** compares film thickness across S1 – S4. Each sample group was fabricated in at least five nominally identical devices to enable reproducibility analysis.

Mechanical and electromechanical measurements were conducted using a custom tensile stage coupled to a digital source meter and a computer-controlled data acquisition system. During sensing measurements, a constant bias voltage of 1 V was applied unless otherwise specified, and the relative resistance change was calculated as $\Delta R/R_0$, where R0 is the initial resistance in the undeformed state.

Table 1: Summary of formulation/process traceability items and structural and chemical characterization parameters of the amorphous silicon-carbon nanocomposite sensing layers.

Parameter	Unit	S1	S2	S3	S4
Film thickness	μm	34.2	36.8	39.4	42.1
Surface roughness R_q	nm	18.3	31.6	44.9	40.5
XRD amorphous halo center	° (2θ)	23.1	23.5	24.0	24.2
Raman I_D/I_G	a.u.	0.82	0.96	1.08	1.19
XPS C/Si atomic ratio	-	1.96	2.56	3.42	4.08
Si-C related bond fraction	%	18.4	24.7	31.2	27.8
C-C/C=C related bond fraction	%	44.6	49.3	54.8	60.5
Si-O-C plus Si-Ox bond fraction	%	37.0	26.0	14.0	11.7
Electrical conductivity	S m^{-1}	0.038	0.084	0.129	0.164
Conductive-domain size	nm	7.8	11.6	15.2	17.9

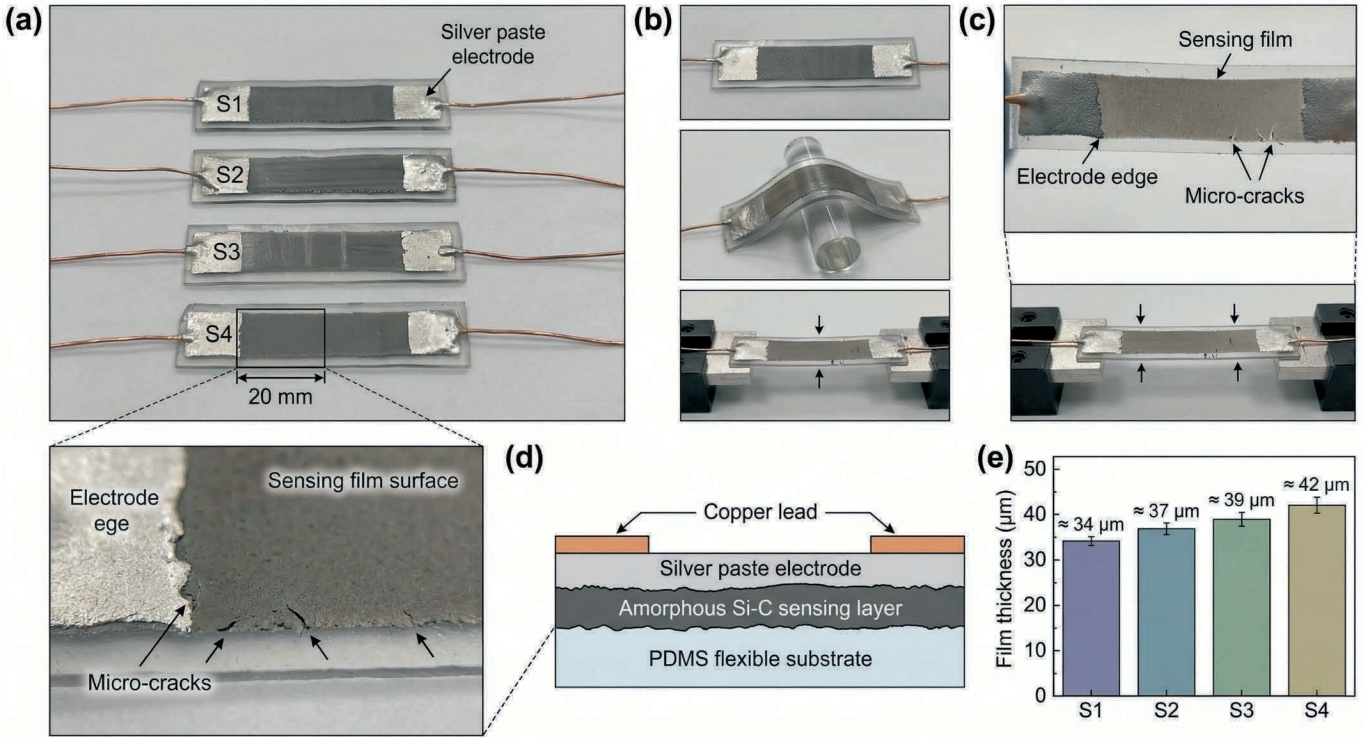

Fig. 1: Macroscopic appearance and geometric configuration of the flexible strain-sensor devices. (a) Photographs of the fabricated S1 – S4 devices under identical viewing conditions. (b) Flexibility demonstration of the representative device in flat, bent, and stretched states. (c) Enlarged view of the sensing region and electrode-transition region. (d) Cross-sectional device architecture showing the substrate, sensing layer, and electrode layout. (e) Quantitative comparison of film thickness across S1 – S4.

The gauge factor (GF) was obtained as the slope of the linear fit to $\Delta R/R_0$ versus strain within each strain interval, using the same 0 – 10%, 10 – 40 %, and 40 – 80 % boundaries for S1, S2, S3, and S4. The reliable working strain range was operationally defined as the largest strain interval over which the response remained monotonic and repeatable without fracture, waveform collapse, or an unrecoverable baseline shift after unloading. Response and recovery times were extracted from the 10 – 90 % and 90 – 10 % transitions of square-wave loading traces, respectively. The hysteresis factor was calculated as the maximum separation between loading and unloading $\Delta R/R_0$ curves divided by the full-scale response at the same strain, expressed as a percentage. Signal-to-noise ratio was calculated from the mean response amplitude divided by the baseline noise level, and the minimum detectable strain was defined as the lowest strain that produced a signal-to-noise ratio of at least 3.

Unless otherwise stated, device-level sensing metrics are reported as mean values from at least five nominally identical devices per group, with repeated loading cycles used to confirm waveform repeatability. Error bars in the corresponding figure panels represent device-to-device standard deviation rather than fitting uncertainty. The comparisons among S1 – S4 are descriptive; no inferential statistical test was used unless a significance threshold is added from the raw replicate data. Peak retention was calculated as the post-cycling peak $\Delta R/R_0$ divided by the initial peak $\Delta R/R_0$ under the same strain condition. Baseline drift was calculated as the absolute baseline-resistance change after cycling divided by the initial baseline resistance. Environmental signal deviation was calculated relative to the signal measured before humidity or thermal exposure.

For chemical-state interpretation, XPS peak fitting was treated as a comparative analysis performed under a consistent fitting protocol for all four samples. The C 1s, Si 2p, and O 1s regions were assigned to C-C/C=C, carbon bonded to silicon or oxygen, Si-C, Si-O-C, and SiOx-related components according to the binding-energy ranges commonly used for amorphous Si-C/SiOC materials. Component areas were normalized within each high-resolution region before comparison across S1 – S4.

SEM crack-density and crack-width values were treated as image-derived descriptors rather than direct proof of a single causal pathway. Crack density was calculated as the number of visible transverse crack openings divided by the analyzed length after 50 % tensile loading, and average crack width was measured from representative crack openings in the same strain state.

III. Results and Discussion

(1) Structural evolution and chemical-state regulation

The first requirement for interpreting the sensing behavior of the four devices was to determine whether the active layers formed tunable amorphous silicon-carbon nanocomposite networks rather than simple carbon-rich coatings with incidental silicon residue. The X-ray diffraction (XRD) patterns collected from S1 to S4, as summarized in **Fig. 2a**, displayed no sharp diffraction peaks attributable to long-range crystalline Si, SiC, or graphitic carbon, but instead showed broad halos centered at 23.1 degrees, 23.5 degrees, 24.0 degrees, and 24.2 degrees, respectively. This gradual shift toward higher 2theta values is consistent with a progressive increase in short-range packing density and carbon-rich domain development while preserving an overall amorphous framework. Such a result agrees with the expected behavior of silicon oxycarbide or amorphous Si-C derived networks, in which local structural rearrangement can occur without the emergence of extended crystallinity [18]. The absence of crystalline diffraction supports the interpretation that the subsequent electromechanical response is unlikely to originate from brittle crystalline-fragment percolation and is more plausibly associated with deformation-induced evolution of disordered conductive paths and local interfacial separation.

Raman spectroscopy further clarified the carbon-domain evolution within the nanocomposite network. As shown in **Fig. 2b**, all samples exhibited the characteristic D and G bands of disordered carbon, while **Fig. 2d** quantifies the increase in the relative intensity ratio ID/IG from 0.82 for S1 to 0.96 for S2, 1.08 for S3, and 1.19 for S4. Meanwhile, the G-band position shifted from 1 581 cm^{-1} in S1 to 1 574 cm^{-1} in S4. This combination of increasing ID/IG and progressive G-band downshift indicates that the conductive carbon domains became more abundant and structurally disordered as carbon enrichment increased. Similar disorder evolution has been reported in amorphous Si-C systems when process conditions favor greater carbon incorporation and local bonding reorganization [15, 16]. In the present system, however, the Raman data suggest that higher carbon content does not simply create a better sensor in a monotonic sense. S4 contained the highest carbon-related signal, yet its eventual sensing performance did not surpass that of S3. This disconnect between carbon abundance and sensing superiority is one of the central findings of the research work. It implies that the most useful conductive network is not the most carbonized one, but the one in which carbon-domain continuity, interfacial anchoring, and strain-responsive path separation remain in balance.

The FTIR spectra shown in **Fig. 2c** support this interpretation, and the summarized band-intensity ratios in **Fig. 3e** make the same trend easier to compare across the four samples. The Si-C related intensity ratio increased from 0.61 in S1 to 0.74 in S2 and 0.86 in S3, then decreased slightly to 0.81 in S4, whereas the Si-O-Si related band ratio declined monotonically from 0.78 to 0.45. The gradual weakening of Si-O-Si signatures together with the strengthening of Si-C associated vibrations indicates that the precursor-derived matrix underwent a meaningful conversion toward a more carbon-linked silicon environment, consistent with literature reports on silane-derived silicon oxycarbide films [13, 14, 18, 19]. However, the slight decline of the Si-C indicator in S4 despite the continued increase in total carbon fraction suggests that the highest-carbon sample did not simply strengthen all beneficial interfacial linkages. Instead, the data are more consistent with the development of a more

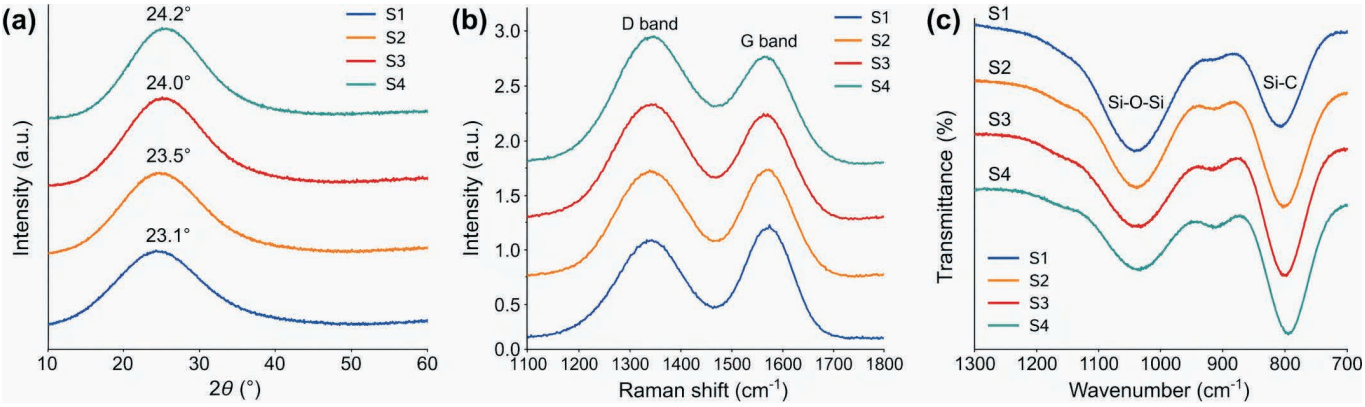

Fig. 2: Structural evolution of the amorphous silicon-carbon network revealed by means of XRD, Raman spectroscopy, and FTIR. (a) XRD patterns of S1 – S4 showing broad amorphous halos without sharp crystalline peaks. (b) Raman spectra with D and G bands marked for the four sensing layers. (c) FTIR spectra highlighting Si-C and Si-O-Si related vibrational regions.

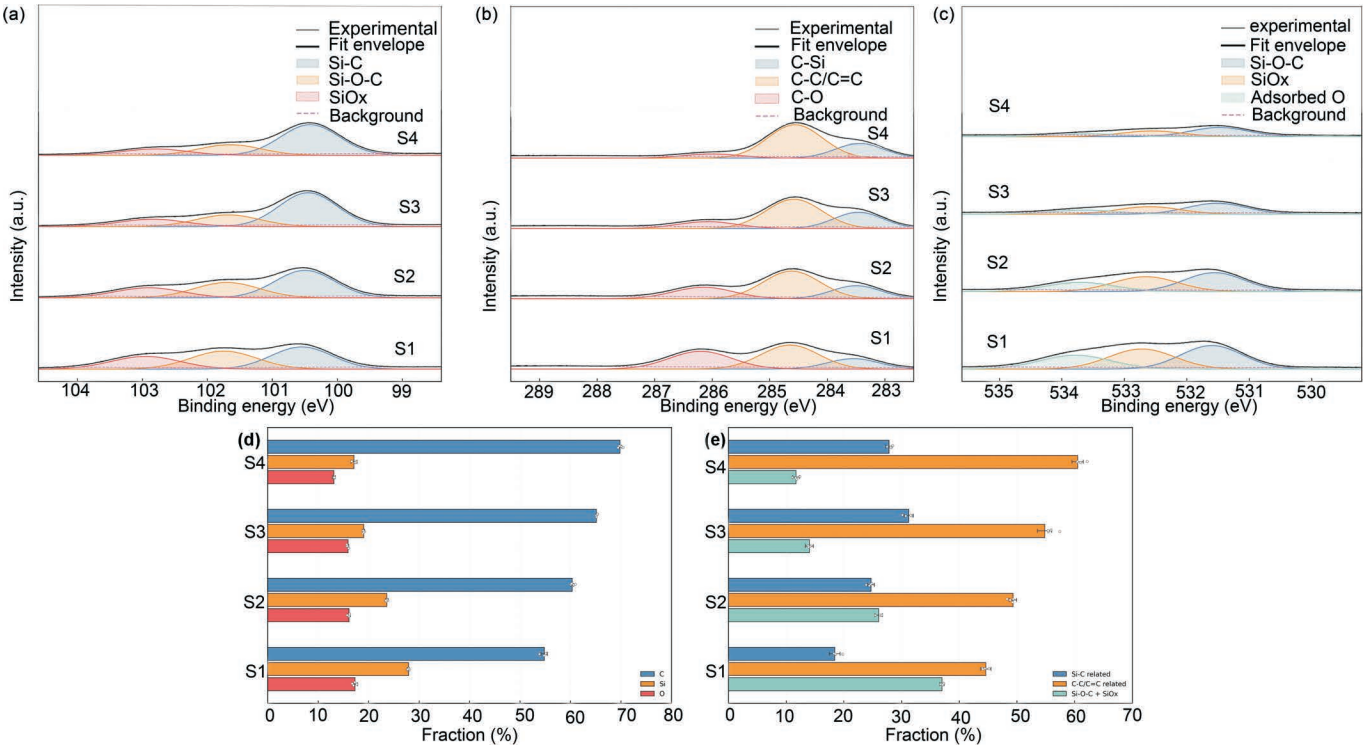

Fig. 3: XPS evidence for chemical-state regulation in the amorphous silicon-carbon nanocomposite sensing layers. (a) High-resolution Si 2p spectra with fitted Si-C and oxygen-containing silicon components. (b) High-resolution C 1s spectra distinguishing C-C/C=C and carbon bonded to silicon or oxygen. (c) High-resolution O 1s spectra showing the decline of oxygen-rich bonding environments across the series. (d) Quantitative comparison of elemental atomic fractions of C, Si, and O. (e) Quantitative comparison of Si-C related, C-C/C=C related, and Si-O-C plus SiOx bond-state fractions.

carbon-dominated but less optimally bonded network, in which additional carbon contributes to baseline conductivity yet does not further improve mechanically coupled path modulation.

The XPS results in **Fig. 3** provide comparative chemical evidence for this structural transition. **Figs. 3a-c** present the fitted high-resolution Si 2p, C 1s, and O 1s spectra, **Fig. 3d** compares the elemental atomic fractions, and **Fig. 3e** summarizes the relative bond-state fractions. The survey spectra showed that C, Si, and O were the principal elements in all four samples, while quantitative deconvolution showed a steady increase in carbon atomic fraction from 54.8 % in S1 to 69.8 % in S4, accompanied by a reduction in silicon from 27.9 % to 17.1 % and oxygen from 17.3 % to 13.1 %. The C/Si atomic ratio therefore rose from 1.96 to 4.08 across the series, consistent with carbon enrichment of the active layer. More importantly, high-resolution spectra showed that the Si-C related bond fraction increased from 18.4 % in S1 to 24.7 % in S2 and 31.2% in S3, but then fell to 27.8 % in S4. By contrast, the C-C/C=C fraction continued increasing to 60.5 % in S4, whereas the combined Si-O-C and SiOx fraction decreased continuously from 37.0 % to 11.7 %. This pattern suggests that S3 occupied the most favorable chemical-state window for forming mechanically anchored conductive pathways.

The chemical trends outlined above help explain why S3 later displayed the best comprehensive sensing behavior. From a conduction standpoint, the rise in the C-C/C=C fraction from S1 to S4 should reduce initial resistance, which indeed occurred. However, high conductivity alone does not guarantee high sensitivity, especially in resistive strain sensors operating through crack opening, tunneling-distance variation, and local pathway interruption. If the network becomes overly carbonized and too structurally stable, mechanical loading may no longer induce sufficiently large relative changes in the effective conduction pathways. In that case the baseline current remains high, but the differential response to strain is muted. S4 closely followed this logic. It exhibited the highest conductivity at 0.164 S m^{-1} and the lowest initial resistance at 4.9 kΩ, yet its gauge factors in all three strain regimes were lower than those of S3. In contrast, S1 contained insufficient conductive connectivity and too large a fraction of oxygen-containing bonding states to generate strong signal amplification. The XPS and FTIR data therefore define the compositional boundaries of the sensing window: insufficient carbon enrichment produces electronically underdeveloped pathways, whereas excessive carbon enrichment can suppress strain-induced path modulation.

Another notable outcome is that the structural and chemical indicators did not evolve independently. The maximum Si-C fraction in S3 coincided with the strongest FTIR Si-C signature and with the later emergence of the most favorable electromechanical balance. This convergence implies that the performance gain in S3 cannot be attributed to one measurement artifact or isolated parameter. Instead, the data consistently indicate that the optimized sample possessed a more effectively cross-linked and mechanically coupled amorphous silicon-carbon network. This point is important when positioning the work against the broader strain-sensor literature. Many high-performance systems rely on purely carbonaceous or metallic conductive skeletons [1,2,7–9], whereas the present results suggest that a silicon-containing amorphous matrix can play an active structural role in controlling interfacial stability and strain transfer, not merely serving as a passive host. The chemical-state analysis therefore sets up the rest of the discussion by showing that the four samples are not arbitrary variants, but members of a deliberately tuned structural series.

The values compiled in **Table 1** further support this interpretation. As S1 transitioned to S3, the increase in Raman disorder, carbon atomic fraction, Si-C associated bonds, and conductivity occurred simultaneously with a decrease in oxygen-rich bonding contributions. Once the network reached S4, continued carbon enrichment no longer translated into further improvement in the chemically beneficial Si-C fraction. This inflection point is where the research locates the optimum. It is therefore reasonable to hypothesize that the performance maximum appears not at the point of highest conductivity, but at the point where chemical-state reconfiguration still supports reversible, deformation-sensitive path evolution. The following morphology and mechanics results are consistent with this hypothesis.

A further point worth emphasizing is that the structural descriptors in **Table 1** are not merely descriptive but are associated with later device behavior. The joint increase in the XRD halo position, the Raman disorder index, and the C/Si atomic ratio from S1 to S3 indicates that the network evolved toward a more compact yet still mechanically compliant conductive medium. At the same time, the reduction of oxygen-rich bonding states suggests that the electrical pathway became less dominated by insulating or weakly conductive linkages. If the research work had relied on only one of these measurements, the interpretation would have remained ambiguous. The significance of the present data is that several independent characterization methods converge on the same optimum sample. This convergence supports, but does not by itself prove, the conclusion that S3 represents a chemically and structurally distinct regime in which conductive carbon domains, silicon-related interfacial bonding, and matrix continuity are jointly optimized.

(2) Surface and nanoscale morphology

The SEM observations reveal how the chemical trends described above manifested in the microstructure of the sensing layers [20–23]. **Figs. 4a-d** compare the surface morphology of S1 – S4 at the same magnification. S1 displayed a relatively smooth yet somewhat discontinuous surface, with sparsely distributed conductive features and a low density of visible heterogeneities. Such a morphology is mechanically compliant, but it does not create many localized strain-concentration sites that could amplify the resistance response during deformation. By contrast, S2 exhibited a more continuous textured network, with conductive domains arranged more densely across the surface and cross-section. S3 showed the most favorable morphology: its surface was neither excessively compact nor randomly aggregated, but instead contained a well-developed interconnected texture with moderate topological heterogeneity and abundant potential crack-initiation sites. S4, however, appeared more compact and locally densified. Although this denser morphology would be expected to lower resistance, it also reduces the extent to which mechanical strain can progressively disrupt or reconfigure the conductive skeleton.

Quantitative image analysis in **Figs. 4e-f** supports these qualitative observations. The crack-precursor density measured after 50 % tensile loading rose from 0.84 mm^{-1} in S1 to 1.73 mm^{-1} in S2 and 2.48 mm^{-1} in S3, then dropped to 1.32 mm^{-1} in S4. At the same strain level, the average crack width increased from 1.7 μm in S1 to 2.3 μm in S2 and 2.6 μm in S3 before decreasing to 1.9 μm in S4. These values are consistent with S3 generating a large number of discrete, mechanically responsive micro-openings without undergoing uncontrolled fracture. If cracks are too sparse, as in S1, the conductive path changes remain too small to generate strong signal amplification. If the network is too dense and mechanically stabilized, as in S4, crack opening becomes more limited and the relative resistance change per unit strain declines. The

peak crack density in S3 therefore provides a morphology-based explanation consistent with its later high gauge factor in the medium- and high-strain regimes.

Cross-sectional SEM images also support the idea that S3 achieved the most favorable structural balance. The sensing layer in S1 appeared thinner and less compactly integrated with the substrate, whereas S2 and S3 showed improved interfacial continuity and a more coherent cross-sectional profile. The measured film thickness increased gradually from 34.2 µm in S1 to 42.1 µm in S4, but thickness alone cannot explain the sensing response because S4 did not outperform S3. Instead, the cross-sectional evidence suggests that the film in S3 combined adequate thickness for stable conductive-path formation with sufficient internal heterogeneity for strain-induced path modulation. This observation is consistent with reports that structural hierarchy, rather than mere loading quantity, often determines the most useful sensor performance [24].

The atomic force microscopy (AFM) data in **Fig. 5** offer an additional layer of evidence by quantifying the surface topography associated with local strain concentration. **Figs. 5a-d** show the AFM height maps, and **Fig. 5e** summarizes the roughness values. The root-mean-square roughness increased from 18.3 nm in S1 to 31.6 nm in S2 and 44.9 nm in S3, before decreasing slightly to 40.5 nm in S4. The three-dimensional AFM reconstructions showed that S1 possessed the flattest surface, whereas S2 and S3 developed increasingly pronounced nanoscale ridges and depressions. Moderate roughness can increase the probability of localized deformation gradients, thereby promoting gradual opening of strain-sensitive conductive gaps. This interpretation has been invoked in other textured or microcrack-assisted systems [20,21], and the present results suggest that a similar effect can be engineered within an amorphous silicon-carbon nanocomposite.

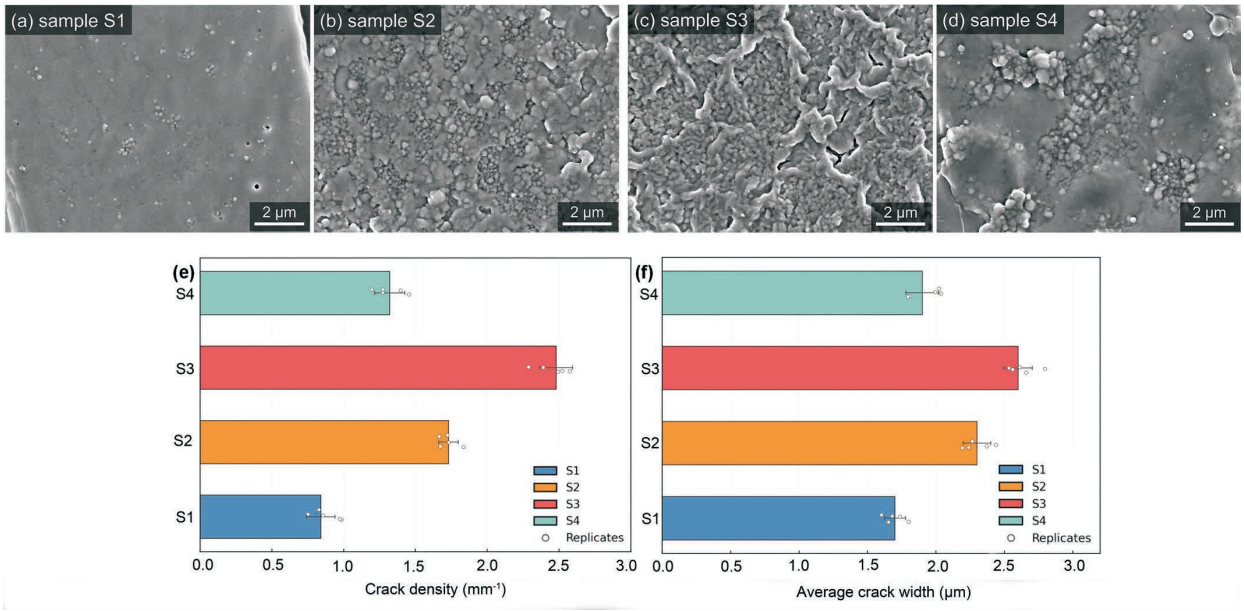

Fig. 4: SEM analysis of surface and cross-sectional morphology in the four nanocomposite sensor groups. (a – d) Surface SEM micrographs of S1, S2, S3, and S4 at identical magnification. (e) Comparison of crack density after 50 % tensile loading. (f) Comparison of average crack width after 50 % tensile loading.

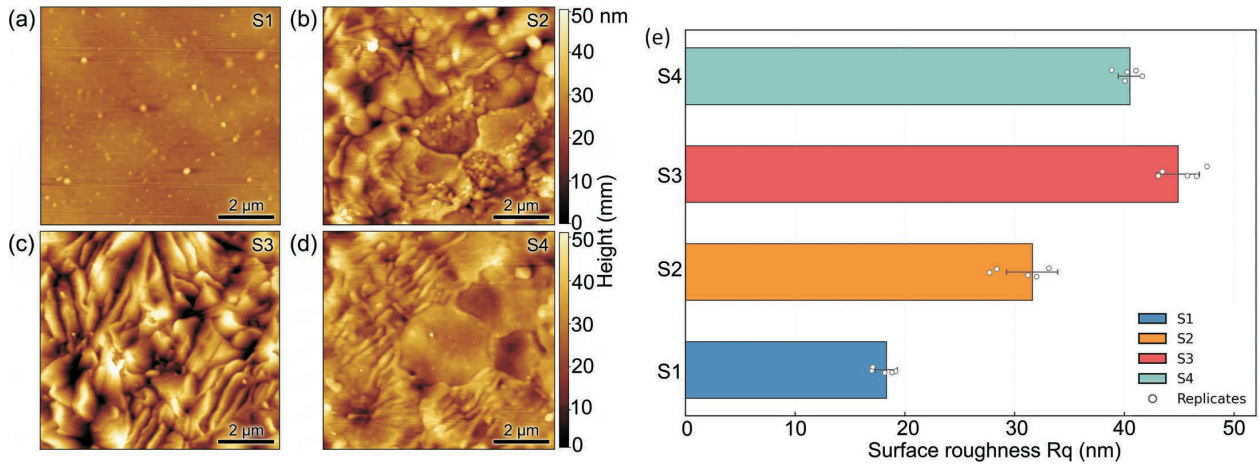

Fig. 5: AFM topography and roughness evolution of the sensing surfaces. (a – d) AFM height maps of S1, S2, S3, and S4. (e) Quantitative comparison of root-mean-square roughness R_q across S1 – S4. These panels demonstrate that moderate surface roughness and topographic heterogeneity are maximized in S3 and contribute to enhanced strain sensitivity.

(3) Mechanical adaptability of the composite sensing layer

Mechanical compliance is a non-negotiable requirement for wearable strain sensors because even excellent electrical sensitivity is of limited value if the sensing layer suffers from premature fracture, excessive residual deformation, or severe mechanical hysteresis. **Fig. 6** compares the mechanical behavior of S1 – S4 and reveals a systematic shift from compliance-dominated to stiffness-dominated behavior across the compositional series. **Fig. 6a** presents the stress-strain curves, **Figs. 6b-d** summarize Young's modulus, tensile strength, and fracture strain, and **Figs. 6e-g** evaluate cyclic mechanical reversibility through loading-unloading loops, residual strain, and energy dissipation. S1 exhibited the lowest Young's modulus at 1.38 MPa and the highest fracture strain at 118 %, confirming that the low-carbon network remained mechanically soft and tolerant of large deformation. S2 and S3 showed moderate increases in modulus to 1.56 and 1.71 MPa, respectively, while maintaining fracture strains of 104 % and 92 %. S4 became the stiffest sample at 1.95 MPa, with the fracture strain reduced to 76 %.

These values indicate that carbon enrichment and network densification strengthened the active layer, but the associated gain in mechanical integrity came at the cost of reduced extensibility. Such a trend is common in conductive nanocomposite sensors [2,9], yet the present data show that the penalty remained manageable up to S3. Although S3 was stiffer than S1 and S2, its fracture strain still exceeded its reliable sensing window of 0 – 90 %, meaning that the device could operate across its full working range without approaching catastrophic structural failure. This is an important distinction. A highly sensitive sensor that only functions near its fracture limit is not suitable for realistic motion capture. By contrast, S3 retained enough mechanical margin to accommodate repeated loading while still benefiting from a comparatively strong electromechanical response.

The tensile strength also increased steadily from 0.86 MPa in S1 to 1.25 MPa in S4, again reflecting improved network reinforcement with carbon enrichment. However, tensile strength alone did not define the best sensing layer. If it did, S4 would have been the preferred device. Instead, the combination of tensile strength, modulus, and fracture strain suggests that S3 offered the most favorable mechanical compromise. It was strong enough to maintain structural continuity during repeated deformation, but not so stiff that deformation-induced pathway evolution was suppressed. This balance becomes clearer when the cyclic mechanical response is examined. After 100 loading cycles at 30 % strain, residual strain decreased from 3.9 % in S1 to 3.1 % in S2 and 2.4 % in S3, before rising slightly to 3.0 % in S4. Similarly, the mechanical energy dissipation ratio declined from 17.8 % in S1 to 11.2 % in S3, then increased to 13.1 % in S4.

The cyclic-mechanics data imply that S3 dissipated the least mechanical energy during repeated loading and unloading, which is consistent with its later low electrical hysteresis. In other words, the optimized sample was not merely a chemically and morphologically favorable structure; it also behaved as the mechanically most reversible network in the operating strain range. S1, despite its large elongation capacity, showed higher energy loss and residual strain, indicating that its soft network underwent more irreversible rearrangement under repeated deformation. S4, despite its higher strength, also showed a rebound in residual strain and energy dissipation, likely because its denser conductive skeleton constrained uniform deformation and promoted localized stress retention. These opposing failure modes again support the notion that the optimum lies in a balanced intermediate structure.

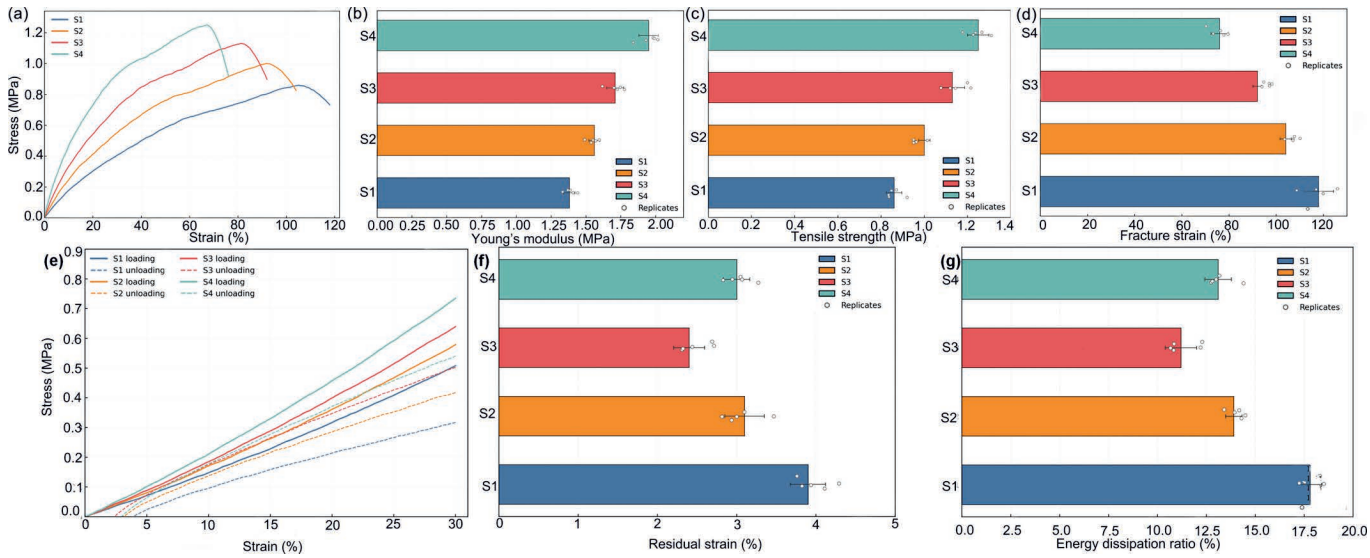

Fig. 6: Mechanical behavior and cyclic mechanical reversibility of the nanocomposite sensing layers. (a) Stress-strain curves of S1 – S4. (b) Comparison of Young's modulus. (c) Comparison of tensile strength. (d) Comparison of fracture strain. (e) Representative cyclic loading-unloading response at 30 % strain. (f) Residual strain after 100 cycles. (g) Mechanical energy dissipation ratio. Together, these panels show that S3 combines sufficient flexibility with the best mechanical reversibility in the operating range.

From an application perspective, this mechanical result is particularly important for sensors intended for repetitive motion capture on curved body surfaces. A device attached to fingers, wrists, elbows, or knees must tolerate thousands of deformation cycles without permanent mechanical distortion, otherwise baseline drift will accumulate rapidly and compromise signal interpretation. The mechanical data suggest that S3 is the most suitable candidate for such use because it combines adequate flexibility with low cyclic mechanical irreversibility. The close agreement between the mechanical reversibility trend and the later electrical stability trend also strengthens the credibility of the proposed sensing mechanism. If electrical hysteresis had improved while mechanical dissipation worsened, the interpretation would have been inconsistent. Instead, both classes of measurement point to the same conclusion: the S3 network provides the most reversible deformation-mediated conductive response. Another useful way to interpret the mechanical data is to compare the gap between fracture strain and reliable sensing range. For S1, that gap was large, indicating that the material could deform well beyond the region in which it generated strong and useful electrical signals. This mismatch is typical of mechanically soft but electronically inefficient sensing layers. For S4, the gap narrowed substantially because the material became stiffer and more constrained, meaning that the sensor approached its structural limit sooner even though its baseline conductivity improved. S3 provided the most practical compromise: the film retained enough mechanical headroom to operate safely within its sensing window, yet the deformation applied within that window was already sufficient to trigger strong and repeatable electromechanical amplification. This margin between operating range and failure threshold is rarely highlighted explicitly, but it is highly relevant to device engineering because it determines whether a sensor can be used conservatively in long-term service rather than only under carefully controlled short-term tests. In that sense, S3 was not merely the best performer in a laboratory comparison; it was also the most mechanically credible device for sustained wearable deployment.

(4) Comparative electromechanical response across sensor groups

The strain-response curves in **Fig. 7** provide the clearest evidence of how structural optimization translated into sensing performance. **Fig. 7a** shows the full-range response curves, **Fig. 7b** enlarges the low-strain region, and **Fig. 7c** presents the segmented linear fitting for the optimized S3 sample. All samples exhibited monotonic increases in relative resistance change with increasing tensile strain, confirming that they operated as positive piezoresistive strain sensors. However, the amplitude and slope of the response differed dramatically across the four groups. At 30 % strain, $\Delta R/R_0$ values were 0.46 for S1, 0.91 for S2, 1.38 for S3, and 1.07 for S4. At 60 % strain, the same values rose to 1.28, 3.42, 5.96, and 4.11, respectively. These data immediately demonstrate two points: First, increasing carbon enrichment from S1 to S3 substantially improved the magnitude of the piezoresistive response. Second, the improvement was not monotonic beyond S3, because S4, despite its lower initial resistance, generated a smaller normalized signal than S3 at both moderate and large deformation.

Segmented gauge-factor analysis in **Figs. 7d-f** makes this trend even more explicit. The 0 – 10 %, 10 – 40 %, and 40 – 80 % intervals were selected to separate low-strain subtle deformation, medium-strain common joint motion, and high-strain large deformation, and the same interval boundaries were applied to all four samples. In the low-strain regime of 0 – 10 %, the gauge factor increased from 6.8 in S1 to 11.9 in S2 and 17.4 in S3 before declining to 13.6 in S4. In the intermediate regime of 10 – 40 %, the gauge factor rose much more sharply, reaching 18.5, 42.7, 73.8, and 51.2 for S1 – S4, respectively. In the high-strain regime of 40 – 80 %, the contrast became strongest: S1 reached 49.6, S2 reached 131.4, S3 reached 286.7, and S4 reached 178.5. Thus, relative to S1, S3 exhibited a 2.56-fold-higher low-strain gauge factor, a 3.99-fold-higher medium-strain gauge factor, and a 5.78-fold-higher high-strain gauge factor.

The response profile of S3 is noteworthy because it remained high without entering the extreme-performance regime reported for specially engineered crack sensors that rely on very narrow operating conditions. Instead, S3 combined a reliable working strain range of 0 – 90 % with high but still credible segmented sensitivity. This places it in a competitive yet defensible position relative to published flexible resistive sensors [1, 2, 5 – 9]. The research work therefore does not depend on claiming a record value. Its scientific contribution is the demonstration that an amorphous silicon-carbon nanocomposite can reach a practically strong performance envelope through coordinated chemical-state regulation and topological control.

Linearity is another important aspect of sensor performance, especially when the device is intended for quantitative motion capture. Over the 0 – 40 % strain range, the linearity coefficient R^2 increased from 0.982 in S1 to 0.988 in S2 and 0.992 in S3, then decreased slightly to 0.984 in S4. The excellent linearity of S3 suggests that the progressive disruption of its conductive pathways occurred in a more regular and repeatable manner than in the other samples. S1 likely suffered from weak percolation changes at small strain, resulting in lower signal contrast, while S4 likely experienced a more complex competition between stable bulk conduction and localized crack opening. This interpretation is fully consistent with the structural evidence described earlier.

The minimum detectable strain shown in **Fig. 7 g** also favored S3. The detection limit decreased from 0.40 % in S1 to 0.25 % in S2 and 0.10 % in S3, then increased slightly to 0.12 % in S4. This value is highly relevant for weak physiological or micro-motion signals. The S3 device was therefore not only better at high-strain amplification, but also more capable of resolving subtle deformation. This dual advantage is uncommon because sensors optimized for large motion often sacrifice low-strain precision. The signal-to-noise ratio at 5 % strain followed the same trend,

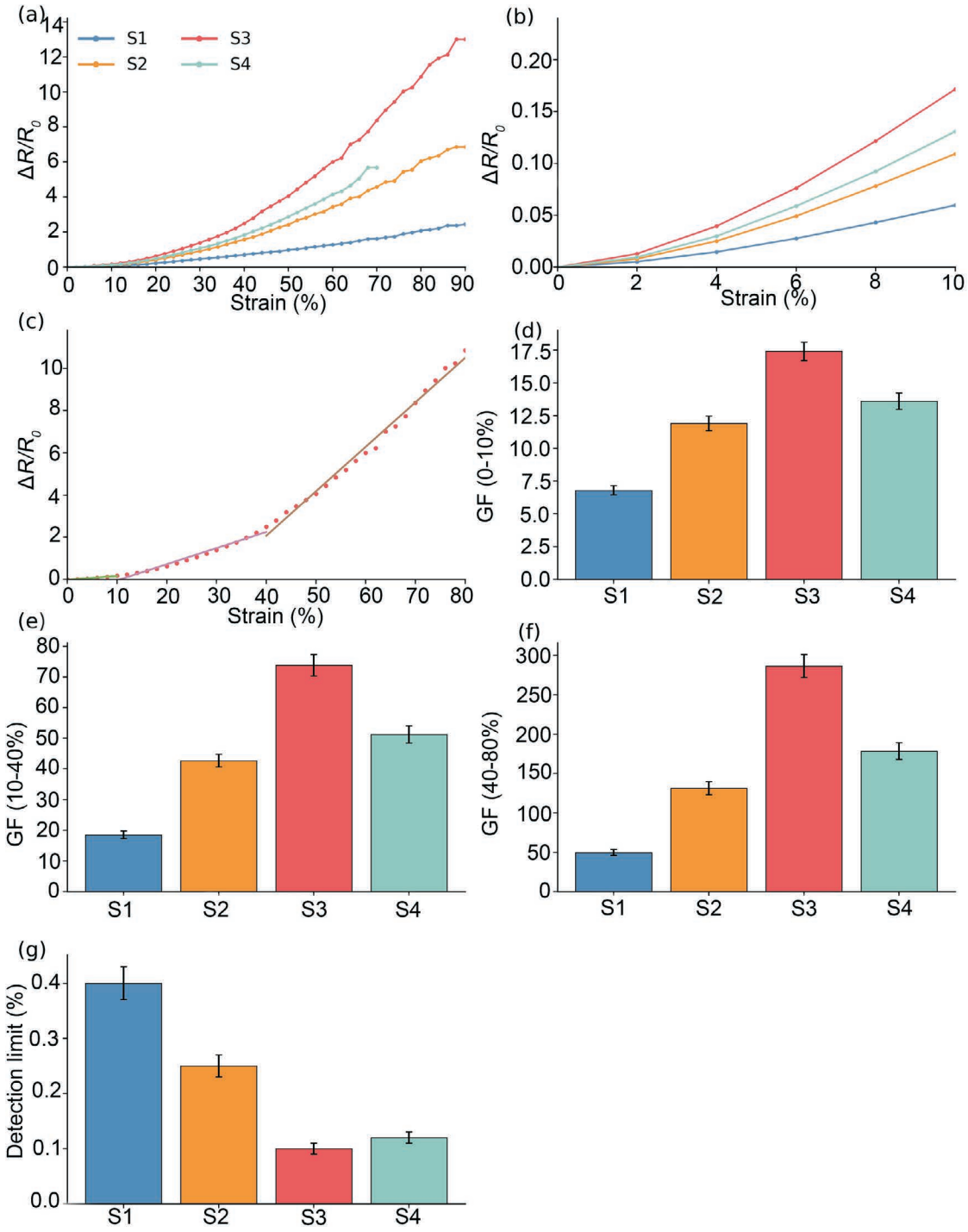

Fig. 7: Comparative electromechanical response and segmented gauge-factor analysis. (a) Relative resistance change versus strain for S1 – S4 over the full working range. (b) Enlarged low-strain response. (c) Segmented linear fitting of S3 in the 0 – 10 %, 10 – 40 %, and 40 – 80 % strain intervals. (d – f) Gauge-factor comparisons for the low-, medium-, and high-strain regimes, respectively. (g) Minimum detectable strain comparison.

increasing from 22.4 dB in S1 to 33.8 dB in S3 before slightly decreasing to 31.5 dB in S4. This confirms that the S3 network amplified useful signal without proportionally increasing noise.

Dynamic testing in **Fig. 8** shows that the superior static performance of S3 was retained under transient loading. **Fig. 8a** presents the S3 response at multiple strain amplitudes, **Fig. 8b** compares the four sensor groups at a fixed amplitude, **Fig. 8d** enlarges one response-recovery cycle, and **Figs. 8e-f** summarize response and recovery times. When subjected to repeated tensile pulses of different amplitudes, all sensors generated repeatable waveforms, but the S3 traces displayed the largest and most distinct amplitude transitions while maintaining a stable baseline. The response time shortened from 124 ms in S1 to 98 ms in S2, 81 ms in S3, and 73 ms in S4. Recovery time followed the same order, falling from 137 ms to 79 ms across the series. S4 was therefore slightly faster than S3, which is reasonable given its lower resistance and more stabilized conductive network. However, this modest

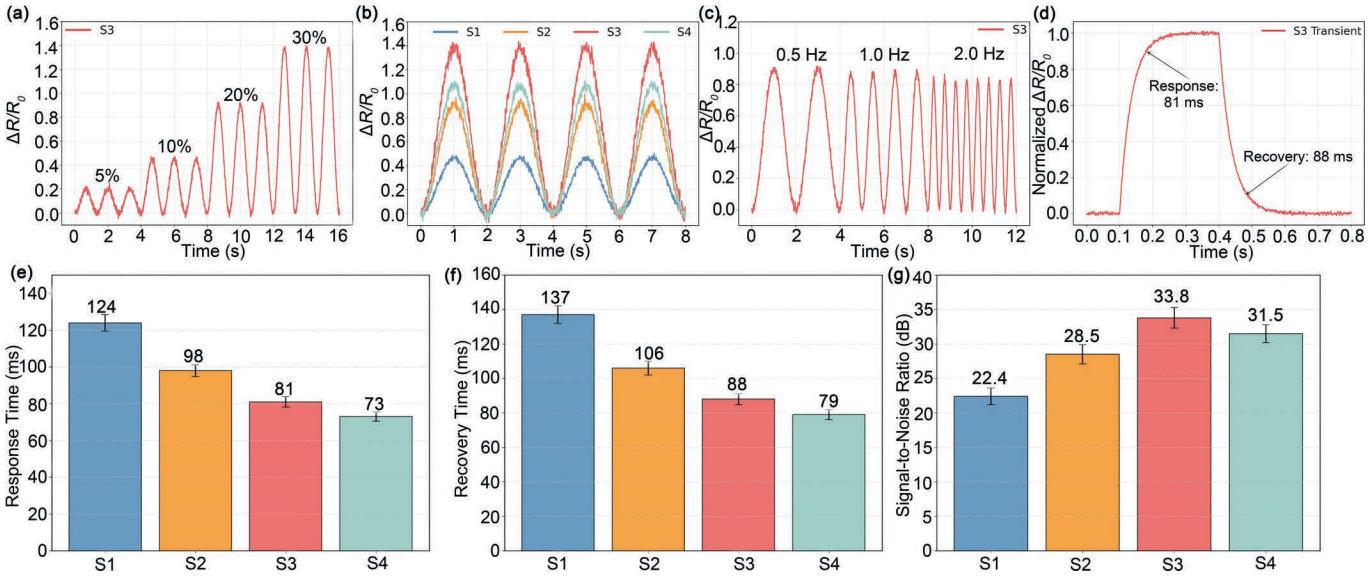

Fig. 8: Dynamic sensing behavior under variable strain amplitudes and loading frequencies. (a) Time-domain response of S3 at multiple strain amplitudes. (b) Comparative dynamic response of S1 – S4 at a fixed strain amplitude. (c) Frequency-dependent response of S3. (d) Enlarged transient response-recovery cycle of S3. (e) Response time comparison. (f) Recovery time comparison. (g) Signal-to-noise ratio at 5 % strain.

kinetic advantage did not compensate for its lower sensitivity, narrower effective strain range, and weaker long-term stability. For motion-capture applications, an 81 ms response time is already fast enough to resolve typical joint motion and many weak body-surface events. Accordingly, the better balance in S3 remains more valuable than the marginal speed gain in S4.

Frequency-dependent measurements in **Fig. 8c** further distinguished the optimized network from the other samples, while the low-strain signal-to-noise ratio summarized in **Fig. 8 g** confirms the noise advantage of S3. The S3 device maintained well-defined waveform profiles across low, medium, and high loading frequencies, with only minor amplitude attenuation. This behavior suggests that the conductive-path reconfiguration in S3 was sufficiently reversible and rapid to track changing strain rates without severe lag. By contrast, S1 showed smaller amplitude changes and less distinct waveform separation, while S4 exhibited slight compression of signal contrast at higher deformation amplitudes, likely because the denser conductive network buffered some of the strain-induced path interruption. Such behavior resembles the limitations observed in practical flexible sensors that prioritize conductivity over deformation-sensitive pathway engineering [25–28].

Taken together, the electromechanical results identify S3 as the sample with the best overall performance and indicate that the optimum is associated with a balanced structural state rather than simple carbon loading. S1 suffered from weak pathway continuity, S2 achieved clear improvement but remained intermediate, S3 combined high segmented sensitivity, low detection limit, high signal-to-noise ratio, and strong linearity, whereas S4 showed that excessive conductivity can reduce the relative sensitivity of the network to deformation. This conclusion is anchored in the structural and chemical data already discussed, although the proposed pathway should be read as a correlation-supported mechanism rather than as direct proof from a single isolated descriptor.

An additional advantage of the segmented response profile is that it makes the device more useful across different classes of human motion. In a purely low-gauge-factor sensor, large motions may remain detectable, but weak motions are often buried in baseline fluctuations. Conversely, in an overly aggressive crack-based sensor, small deformations may be resolved at the expense of unstable responses under repeated large-amplitude loading. The S3 device avoided both extremes. Its low-strain sensitivity enabled clear detection of subtle deformation, while its medium- and high-strain gauge factors increased strongly enough to preserve signal separation during larger excursions. This type of strain-dependent amplification is particularly desirable in motion-capture scenarios in which the same sensor may be mounted on different anatomical locations or used under different postures. It also supports the use of a single materials platform for multimodal deformation monitoring rather than forcing the designer to select one sensor for micro-strain and another for larger joint strain. In that sense, the segmented response is not a complication that must be mathematically corrected; it is a functional feature of the optimized amorphous silicon-carbon network. **Table 2** makes this relationship especially transparent because it compresses the electromechanical response into a format that can be compared directly across low, medium, and high strain windows. The table shows that S3 was not narrowly optimized for only one operating interval. Rather, it outperformed the other samples in a distributed way: its low-strain sensitivity supported subtle-motion detection, its medium-strain response provided good linearity for common joint motion, and its high-strain amplification enabled large-deformation tracking without complete signal saturation. This cross-window balance is more meaningful than a single headline gauge factor because wearable motion capture rarely

occurs in one fixed strain regime. A sensor attached to the body may experience a weak facial strain one moment and a large joint excursion the next. The segmented data therefore reinforce the practical importance of the optimized amorphous silicon-carbon architecture.

Table 2: Electromechanical sensing properties of the four strain-sensor groups. Values are mean values from at least five devices unless otherwise stated; corresponding figure error bars represent device-to-device SD.

Parameter	Unit	S1	S2	S3	S4
Initial resistance	kOhm	19.6	11.4	6.8	4.9
Reliable working strain range	%	0 – 100	0 – 95	0 – 90	0 – 70
Gauge factor at 0 – 10 % strain	-	6.8	11.9	17.4	13.6
Gauge factor at 10 – 40 % strain	-	18.5	42.7	73.8	51.2
Gauge factor at 40 – 80 % strain	-	49.6	131.4	286.7	178.5
Linearity over 0 – 40 % strain	R^2	0.982	0.988	0.992	0.984
Response time	ms	124	98	81	73
Recovery time	ms	137	106	88	79
Hysteresis factor at 40 % strain	%	10.8	8.1	5.6	7.4
Minimum detectable strain	%	0.40	0.25	0.10	0.12

To make the structure-property argument more explicit, this interpretation distinguishes measured descriptors from inferred mechanistic links. The measured facts are that S3 combined the maximum Si-C related bond fraction (31.2 %), the highest measured roughness (R_q = 44.9 nm), the highest crack density after 50 % tensile loading (2.48 mm^{-1}), and the lowest hysteresis factor (5.6 %) among the four groups. The inferred mechanism is that this combination supports reversible conductive-path separation and reconnection more effectively than the under-connected S1 network or the over-stabilized S4 network. This interpretation is therefore presented as a correlation-supported mechanistic explanation rather than as direct proof of a single controlling variable.

(5) Durability, hysteresis, and long-term stability

For wearable motion-capture devices, sensitivity is only useful if it can be preserved under repeated operation. **Fig. 9** therefore examines cycle durability and hysteresis behavior at the panel level through representative cyclic waveforms (**Fig. 9a**), retention curves and summary bars (**Figs. 9b-d**), hysteresis loops (**Fig. 9e**), hysteresis-factor comparison (**Fig. 9f**), and baseline-drift comparison (**Fig. 9g**). The long-cycle results show that all samples retained measurable functionality after repeated loading, but the retention and drift characteristics varied considerably. After 5 000 tensile cycles at 30 % strain, peak signal retention was 87.6 % for S1, 92.8 % for S2, 96.1 % for S3, and 91.4 % for S4. After 10 000 cycles, the values declined to 80.2 %, 88.5 %, 93.3 %, and 86.7 %, respectively. These numbers indicate that S3 preserved its electromechanical response far better than the other devices over prolonged operation.

The superiority of S3 becomes even clearer when baseline drift is considered. After 5 000 cycles, baseline drift reached 9.7 % in S1, 6.2 % in S2, 3.8 % in S3, and 5.4 % in S4. This result mirrors the earlier mechanical reversibility data. The optimized sample underwent the least irreversible mechanical rearrangement and also exhibited the smallest long-term electrical drift. S1, by contrast, showed the largest drift, which is consistent with its less developed conductive network and higher cyclic mechanical dissipation. S4 again occupied an intermediate position. Its denser network resisted catastrophic degradation better than S1, but it did not maintain the same reversible path reconstruction as S3. The data therefore suggest that both underdeveloped and over-stabilized networks can compromise long-term sensing fidelity, albeit through different mechanisms.

Electrical hysteresis followed a similarly non-monotonic trend. At 40 % strain, the hysteresis factor decreased from 10.8 % in S1 to 8.1 % in S2 and 5.6 % in S3, then increased to 7.4 % in S4. The low hysteresis of S3 is particularly significant because highly sensitive resistive sensors often suffer from pronounced loading-unloading mismatch due to irreversible crack growth or delayed structural recovery [20,21]. In the present work, the low hysteresis indicates that the conductive pathway changes in S3 were predominantly reversible over the tested strain range. This reversibility is essential for quantitative interpretation of motion trajectories, where the same physical deformation should ideally generate the same electrical response regardless of whether the motion is part of loading or unloading.

Storage and environmental stability summarized in **Figs. 10a-d** also favored the optimized network. After 30 days of storage, retention remained at 94.2 % for S3, compared with 84.5 %, 90.1 %, and 88.9 % for S1, S2, and S4, respectively. Under 75 % relative humidity, signal deviation reached 8.4 % in S1, 6.1 % in S2, 4.2 % in S3, and 6.8 % in S4. At 60 °C, the corresponding deviations were 7.9 %, 5.4 %, 3.9 %, and 5.7 %. These results indicate that S3 was not only electrically stable but also less sensitive to environmental perturbation. Because humidity and temperature can alter interfacial conductivity, polymer relaxation, and local tunneling conditions, their relatively small effect on S3 suggests that its network architecture remained well coupled under realistic operating conditions. This feature enhances the practical value of the device for wearable use, where ambient conditions are rarely constant [27,29].

Bending endurance and batch reproducibility shown in **Fig. 10e-f** further support the same conclusion. After 2 000 bending cycles at a radius of 2 mm, retention was 95.4 % for S3, exceeding the values of 85.1 %, 91.0% , and 90.6 % for S1, S2, and S4. The batch-to-batch coefficient

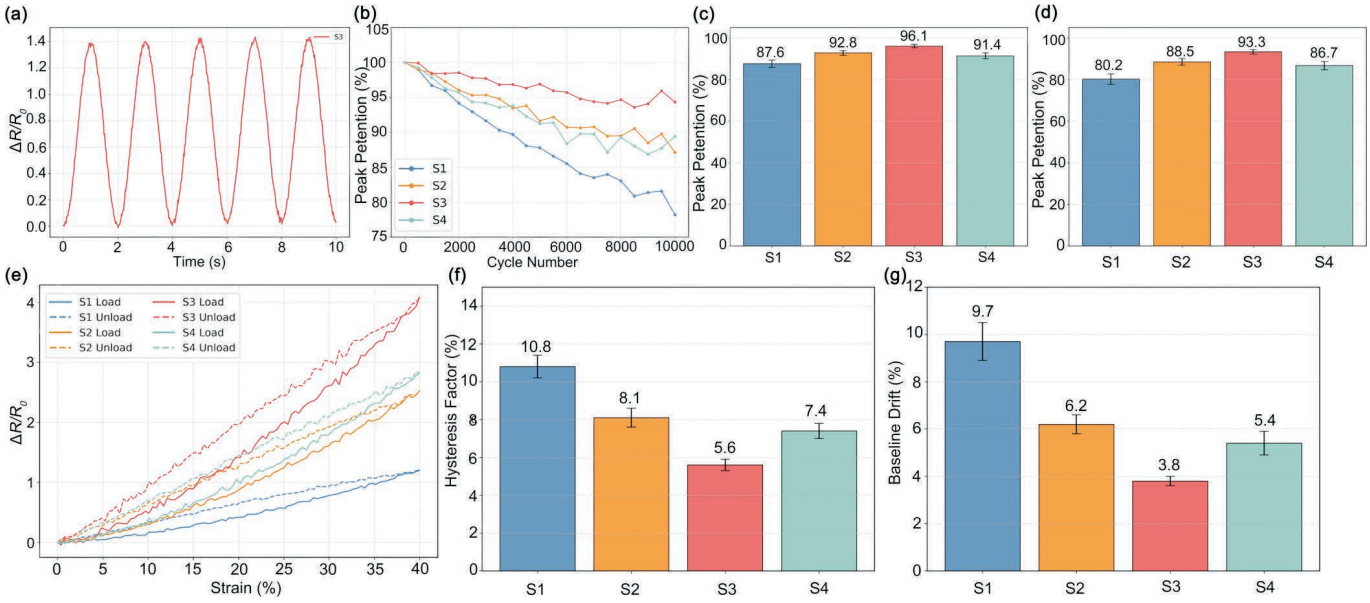

Fig. 9: Long-term durability and hysteresis characteristics of the flexible strain sensors. (a) Representative cyclic waveform window during repeated loading. (b) Peak-retention curves as a function of cycle number. (c) Peak retention at 5 000 cycles. (d) Peak retention at 10 000 cycles. (e) Loading-unloading hysteresis loops at 40% strain. (f) Hysteresis-factor comparison. (g) Baseline drift after long-cycle testing.

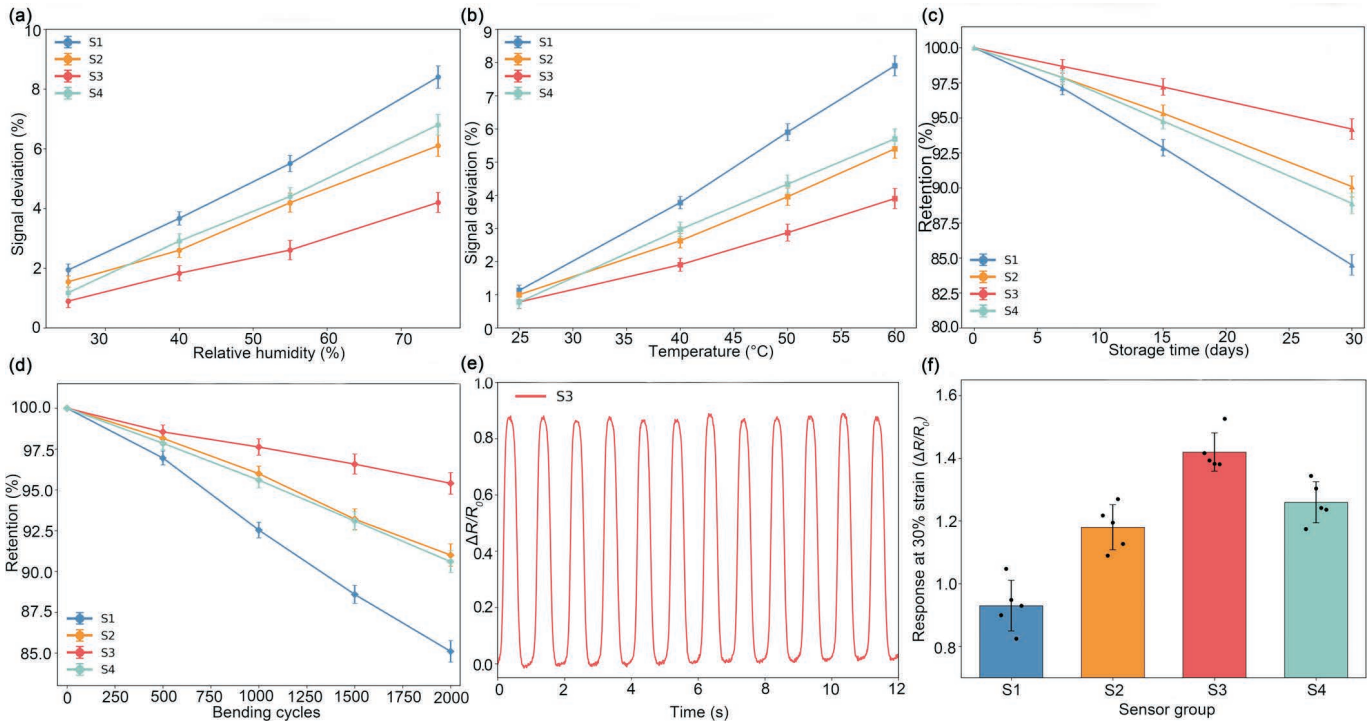

Fig. 10: Environmental robustness, bending endurance, and reproducibility of the nanocomposite strain sensors. (a) Humidity-dependent signal deviation. (b) Temperature-dependent signal deviation. (c) Storage retention after 30 days. (d) Retention after repeated bending. (e) Representative bending-cycle trace of the optimized sensor. (f) Batch-to-batch variation of device response.

of variation was also lowest for S3 at 4.3 %, compared with 8.7 %, 6.1 %, and 5.2 % for the other samples. This suggests that the optimized processing condition not only produced the best single device but also yielded the most reproducible network architecture. Reproducibility is frequently underreported in flexible sensor studies, yet it strongly influences whether a material system can transition from laboratory demonstration to practical manufacturing [22, 25, 26]. The lower variation observed for S3 implies that the optimized amorphous silicon-carbon network forms within a reasonably robust processing window rather than requiring highly unstable conditions.

When the durability data are compared with representative literature, the present system occupies a useful middle ground. It does not claim the extreme gauge factors associated with aggressively cracked networks [1], but it achieves a much better overall balance of cycle stability, low hysteresis, and environmental tolerance than

would be expected from a purely sensitivity-driven design. This balance is particularly important for motion capture, where sensors are repeatedly deformed under variable temperature, humidity, and strain-rate conditions. In that context, a slightly lower but more reproducible signal is often more valuable than a spectacular but unstable one.

Table 3: Reliability, environmental stability, and reproducibility of the four sensor groups. Retention, drift, and environmental deviation are defined in the Methods and table note.

Parameter	Unit	S1	S2	S3	S4
Peak retention after 5 000 cycles at 30 % strain	%	87.6	92.8	96.1	91.4
Peak retention after 10 000 cycles at 30 % strain	%	80.2	88.5	93.3	86.7
Baseline drift after 5 000 cycles	%	9.7	6.2	3.8	5.4
Signal deviation at 75 % RH	%	8.4	6.1	4.2	6.8
Signal deviation at 60 °C	%	7.9	5.4	3.9	5.7
Retention after 30-day storage	%	84.5	90.1	94.2	88.9
Retention after 2 000 bending cycles at 2 mm radius	%	85.1	91.0	95.4	90.6
Batch-to-batch coefficient of variation	%	8.7	6.1	4.3	5.2

It is also useful to consider the likely degradation pathways that differentiate the four samples during long-term operation. In S1, the main failure mode is expected to be progressive rearrangement of an insufficiently interconnected conductive network, leading to cumulative baseline drift and signal attenuation. In S4, by contrast, the main issue is not weak initial conductivity but the reduced reversibility of a denser network in which repeated deformation may induce localized stress concentration and partial conductive-path locking. S2 lies between these two cases and therefore behaves as a competent but not fully optimized sensor. S3 appears to suppress both failure routes simultaneously: it contains enough conductive redundancy to avoid under-percolation and enough structural compliance to prevent over-constrained deformation. This dual suppression explains why the same sample performs best in both cyclic and environmental tests. The values collected in **Table 3** further suggest that the stability advantage of S3 was not an isolated consequence of any single test protocol. The same sample led in cyclic retention, baseline stability, storage durability, humidity tolerance, temperature tolerance, bending endurance, and fabrication reproducibility. Such consistency argues against the possibility that the superior performance of S3 arose from a favorable but statistically unstable specimen. Instead, it indicates that the optimized processing condition produced a network that was intrinsically more robust across multiple kinds of perturbation. This is particularly important for wearable strain sensors because their service environment combines mechanical cycling with thermal fluctuation, moisture exposure, and repeated flexure. A device that performs well under only one of these stresses may still fail in realistic use. The fact that S3 remained dominant across all of them provides a stronger engineering case than a purely sensitivity-focused analysis could offer. It also supports this paper's broader claim that balanced network design improves not only instantaneous response but also operational reliability.

(6) Literature positioning and practical motion-capture demonstrations

The benchmark comparison in Table 4 places the optimized S3 device in the context of representative flexible strain sensors reported in the literature. Compared with the cotton-thread-based sensor reported by Li *et al.* [3], the present device delivers a substantially higher gauge factor over broader medium- and high-strain regimes while retaining comparable practical suitability for wearable monitoring. Relative to the carbon black-silver nanocomposite reported by Zhang *et al.* [23], S3 offers a stronger segmented response and richer materials-level interpretation. Compared with highly engineered crack-based systems such as the one reported by Zhou *et al.* [32], the present sensor does not attempt to compete on ultrahigh extreme-strain gauge factor, but instead emphasizes a more balanced performance envelope including low hysteresis, strong 10 000-cycle retention, and environmental robustness. This positioning is deliberate. The present work is aimed at credible high-performance motion capture rather than at achieving the most dramatic single-metric record.

The comparison with more recent carbon-network and hybrid nanocomposite sensors is especially instructive. Reported gauge factors around 33 to 64 with strain windows between roughly 60 % and 300 % are common in practical flexible resistive sensors designed for wearable body monitoring [16,21]. More aggressive crack or structural-gradient strategies can yield far larger values, but they often do so under highly specialized architectures [34]. The S3 sensor, with a gauge factor of 17.4 at 0 – 10 % strain, 73.8 at 10 – 40 % strain, and 286.7 at 40 – 80 % strain, occupies a strong intermediate regime in which sensitivity is substantially enhanced yet the working strain range remains wide enough for realistic limb motion. Equally important, its response time of 81 ms and 10 000-cycle retention of 93.3 % compare favorably with many practical wearable systems [15,22,24].

A particularly relevant point of comparison is the recent silicon-related flexible sensor based on laser-induced 3C-SiC and carbon allotropes embedded in a soft polymeric network [11]. That study demonstrated that

Table 4: Comparison of the optimized S3 sensor with representative wearable strain sensors reported in the literature. Reference numbers correspond to the reference list.

Material system	Gauge factor	Working strain range	Response time	Cycle life	Application	Reference
Tissue-paper-based flexible resistive sensor	8.7 at 0 – 4 %, 18.5 at 8 – 10 %	up to 10 %	stable at 0.01 – 10 Hz	2 000 cycles	motion and pulse monitoring	3
Carbon black-silver nanoparticle composite	21.12	100 %	not emphasized	repeated motion tests	finger, wrist, elbow	23
Crack-based stretchable sensor	428.5 at 0 – 100 %, much higher at larger strain	up to 300 %	about 70 ms	over 10 000 cycles	motion monitoring	32
MWCNT-PDMS composite film	33.08	0 – 60 %	62 ms	repeated cyclic tests	wearable sensing	21
CNF-CNT-silicone rubber printed sensor	64.32	about 300 %	not emphasized	durable tensile testing	body monitoring	16
Hybrid PDMS-based nanocomposite	221	practical tensile window	130 ms	repeated use	wearable electronics	33
Present S3 sensor	17.4 at 0 – 10 %, 73.8 at 10 – 40 %, 286.7 at 40 – 80 %	0 – 90 %	81 ms	10 000 cycles with 93.3 % retention	motion capture from weak to large deformation	This work

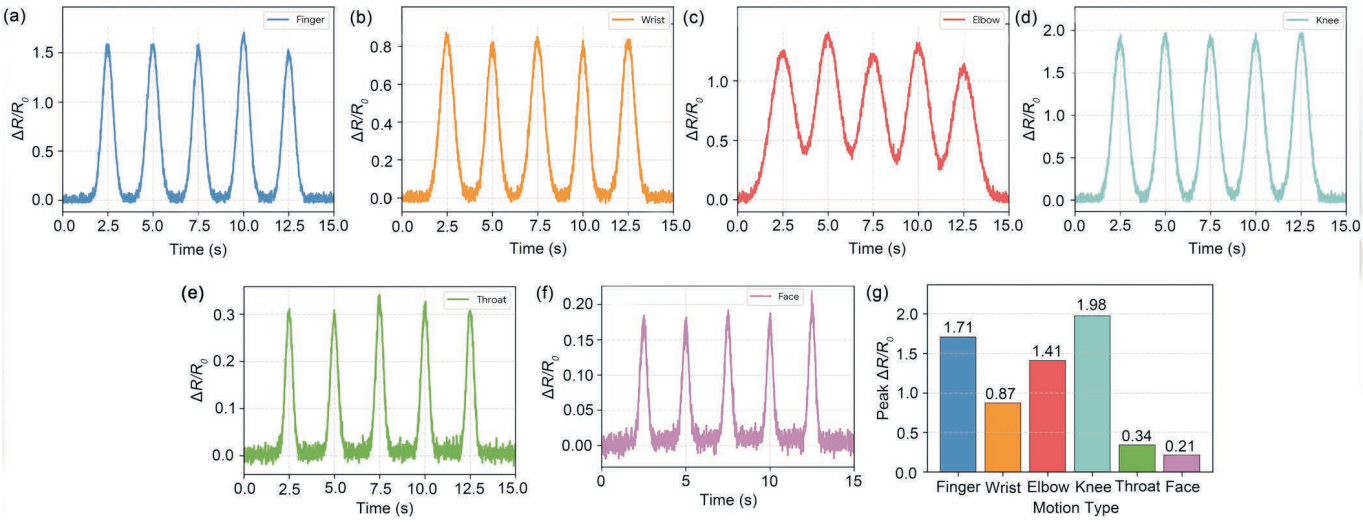

Fig. 11: Demonstration of wearable motion capture using the optimized S3 sensor. (a) Finger-bending monitoring. (b) Wrist-flexion monitoring. (c) Elbow-motion monitoring. (d) Knee-bending monitoring. (e) Throat-motion monitoring. (f) Facial-expression monitoring. (g) Cross-motion peak-signal comparison.

silicon-containing conductive architectures can indeed be adapted to wearable sensing, but it focused on a different structural concept in which crystalline or partially ordered silicon carbide features coexist with carbon allotropes. The present study instead addresses a more chemically and structurally tunable amorphous silicon-carbon nanocomposite. By showing how an amorphous mixed-bond network can be optimized through comparative material characterization, the current work expands the design space for silicon-containing wearable strain sensors beyond crystalline SiC-based approaches.

The application demonstrations in **Fig. 11** further confirm the practical relevance of the optimized S3 device, especially in light of the broader wearable-motion literature on graphene, textile, crack-assisted, and hybrid flexible sensors [35, 36]. **Figs. 11a-d** show representative responses for finger, wrist, elbow, and knee motion, respectively, while **Figs. 11e-f** present the lower-

amplitude throat and facial-expression signals. When attached to the finger, the sensor produced a stable peak $\Delta R/R_0$ of approximately 1.52 during repeated bending cycles. The waveform amplitude remained highly consistent across five consecutive motions, indicating good repeatability and clear distinction between bending and relaxation states. Wrist flexion generated a lower but still distinct amplitude of about 0.84, which is appropriate because the local deformation imposed on the sensor was smaller than during finger bending. Elbow bending yielded a broader waveform with a peak around 1.21, reflecting both the larger motion arc and the slower relaxation dynamics of the tested joint. Knee bending produced the largest amplitude among the major joint demonstrations, reaching approximately 1.87, thereby confirming that the sensor could handle large mechanical excursions without waveform collapse.

The low-strain application results were equally important. During swallowing-related throat motion, the S3 device produced repeatable signals with peak amplitudes around 0.29. Although this value was much smaller than the response to knee or finger bending, it remained easily distinguishable from the baseline because the minimum detectable strain was only 0.10 % and the low-strain signal-to-noise ratio was high. A similar argument applies to facial-expression monitoring, where the peak signal was about 0.17. These results show that the same device could resolve both high-amplitude and subtle deformation, which is a strong indication that the segmented gauge-factor profile was practically useful rather than merely a mathematical artifact.

The multi-motion demonstrations, together with the cross-motion amplitude comparison in **Fig. 11 g**, also illustrate why the optimized sensor is better described as versatile than simply sensitive. A wearable device intended for real-world motion capture must be able to differentiate among motions with different amplitudes, durations, and strain rates. The stable separation among finger, wrist, elbow, knee, throat, and facial-expression waveforms suggests that S3 offers sufficient amplitude resolution and temporal fidelity for that purpose. Moreover, the fact that these demonstrations were achieved without any invasive or ethically sensitive protocol strengthens the translational relevance of the system. The sensor can already be framed as suitable for non-invasive motion capture, gesture recognition, and soft-interface input scenarios.

For the wearable demonstrations in **Fig. 11**, the S3 sensor was surface-mounted on the finger, wrist, elbow, knee, throat, and facial region using a removable non-invasive attachment method, and the response was recorded during repeated voluntary motions after the baseline had stabilized. The same optimized device type was used for the demonstrations, with the sensor allowed to return to baseline between motion sets.

Overall, the literature comparison and application demonstrations reinforce the main contribution of the work. The novelty is not that the present sensor exceeds every published value, but that it establishes a coherent structure-property-performance pathway for amorphous silicon-carbon nanocomposite strain sensors. Rich materials characterization, multi-sample comparison, credible benchmark positioning, and practically relevant demonstrations together create a stronger scientific case than a single extreme sensitivity figure would provide.

From the perspective of wearable-system integration, these demonstrations indicate that the optimized sensor could plausibly support more than simple waveform display. Because the amplitude hierarchy among finger, wrist, elbow, knee, throat, and facial-expression signals remained well separated, the output would be amenable to threshold-based classification or lightweight pattern-recognition methods in future work.

IV. Conclusions

In summary, a comparative study of four amorphous silicon-carbon nanocomposite strain sensors demonstrated that high-performance motion-capture behavior emerges from a balanced conductive network rather than from maximum carbon enrichment alone. Multi-scale characterization confirmed that all sensing layers remained predominantly amorphous, while progressive carbon enrichment from S1 to S4 altered Raman disorder, Si-C related bonding, elemental composition, nanoscale conductive-domain development, surface roughness, and strain-induced crack evolution in a systematic manner. Among the four samples, S3 showed the most favorable combination of structural and chemical features, including the highest Si-C related bond fraction, the most effective roughness level, and the greatest crack density under controlled tensile loading without evidence of uncontrolled structural failure.

These materials characteristics were associated with superior sensing behavior. S3 exhibited a low-strain gauge factor of 17.4, a medium-strain gauge factor of 73.8, and a high-strain gauge factor of 286.7 within a reliable working range of 0 – 90 %, together with high linearity, a minimum detectable strain of 0.10 %, a response time of 81 ms, low hysteresis, and retention of 93.3 % after 10 000 cycles. In contrast, S1 remained mechanically compliant but electrically underdeveloped, whereas S4 achieved higher baseline conductivity and faster response at the cost of weaker strain-amplification efficiency and lower long-term stability than S3. The results therefore suggest that the most useful amorphous silicon-carbon nanocomposite sensor is obtained when conductive continuity, interfacial bonding, surface topology, and reversible path reconfiguration are simultaneously balanced.

The practical demonstrations further indicated that the optimized device can resolve both large joint movement and subtle body-surface deformation, including finger, wrist, elbow, and knee motion as well as throat and facial-expression signals. This versatility, combined with the rich structure-property analysis presented here, suggests that amorphous silicon-carbon nanocomposites constitute a promising platform for wearable motion-capture electronics. Future work may focus on refining encapsulation against long-term environmental drift, expanding large-area fabrication consistency, and integrating signal-processing modules for multimodal intelligent sensing.

References

1 Hanif, A., Kim, D.S.: Micro/Nanofibers for flexible, stretchable, and strain-insensitive wearable electronics: A review, *Adv. Sens. Res.*, **4**, 2400133, (2025).

2 Huang, W., Dong, X., Cai, Y.: Wearable and flexible electronic strain sensor, *Chin. Sci. Bull.*, **62**, 635 – 649, (2017).

3 Li, Y., Samad, Y.A., Taha, T., Cai, G., Fu, S.Y., Liao, K.: Highly flexible strain sensor from tissue paper for wearable electronics, *ACS Sustain. Chem. Eng.*, **4**, 4288 – 4295, (2016).

4 Cai, G., Yang, M., Xu, Z., Liu, J., Tang, B., Wang, X.: Flexible and wearable strain sensing fabrics, *Chem. Eng. J.*, **325**, 396 – 403, (2017).

5 de Almeida Silva, M., Romagnoli, É.S., Carvalho Pereira, R.D., Tarley, C.R.T., Segatelli, M.G.: Structure and porosity of silicon oxycarbide/carbon black composites, *Mater. Chem. Phys.*, **254**, 123503, (2020).

6 Duan, L., Ma, Q., Chen, Z.: Preparation and characterization of mesoporous silicon oxycarbide ceramics without free carbon from polysiloxane, *J. Eur. Ceram. Soc.*, **33**, 841 – 846, (2013).

7 Hansda, S., Sarkar, D., Kundu, S., Kar, A., Bera, S., Das, S., *et al.*: Structural and optical properties of silicon oxycarbide thin films using silane based precursors via sol-gel process, *Thin Solid Films*, **791**, 140226, (2024).

8 Huang, L., Zhang, Y., Zhang, P., Li, Y., Huang, X., Guo, C.: Highly sensitive flexible resistive strain sensor based on swelling-coating method for wearable electronics, *IEEE Sens. J.*, **24**, 21369 – 21377, (2024).

9 Huck, H., Halac, E.B., Oviedo, C., Zampieri, G., Pregliasco, R.G., Alonso, E.V., *et al.*: Characterization of amorphous carbon rich $Si_{1-x}C_x$ thin films obtained using high energy hydrocarbon ion beams on si, *Appl. Surf. Sci.*, **141**, 141 – 147, (1999).

10 Juárez-Olivos, G., Garnica-Palafox, I.M., Islas, S.R., Sánchez-Arévalo, F.M.: Flexible strain sensor based on laser-induced 3C-SiC and carbon allotropes embedded within a soft poly(dimethylsiloxane) polymeric network, *ACS Appl. Electron. Mater.*, **7**, 9922 – 9935, (2025).

11 Kim, N., Park, S., Kim, M.C., Choi, Y.W.: Auxetic crack-based wearable strain sensor designed for sustainable conformal contact, *Sens. Actuators A Phys.*, **387**, 116429, (2025).

12 Kroll, P.: Modeling the "free carbon" phase in amorphous silicon oxycarbide, *J. Non-Cryst. Solids*, **351**, 1121 – 1126, (2005).

13 Xia, J., He, L., Lu, Z., Song, J., Wang, Q., Liu, L., *et al.*: High performance strain sensor based on carbon black/graphene/Ecoflex for human health monitoring and vibration signal detection, *ACS Appl. Nano Mater.*, **6**, 19279 – 19289, (2023).

14 Xu, K., Lu, Y., Takei, K.: Multifunctional skin-inspired flexible sensor systems for wearable electronics, *Adv. Mater. Technol.*, **4**, 1800628, (2019).

15 Xu, M., Yue, Y., Lu, Y., Xiang, K., Wang, J., Lu, W., *et al.*: Three-dimensional printed cellulose nanofibers/carbon nanotubes/silicone rubber flexible strain sensor for wearable body monitoring, *J. Mater. Chem. C*, **12**, 5972 – 5984, (2024).

16 Yang, C., Zhang, D., Wang, D., Chen, X., Luan, H.: Ultra-sensitive, stretchable, and bidirectional wearable strain sensor for human motion detection, *J. Mater. Chem. C*, **10**, 7076 – 7086, (2022).

17 Yang, J., Ling, K., Liu, L., Zeng, X., Xu, X., Li, Z., *et al.*: Printable and wearable graphene-based strain sensor with high sensitivity for human motion monitoring, *IEEE Sens. J.*, **22**, 13937 – 13944, (2022).

18 Su, C.C., Liu, T., Chang, N.K., Wang, B.R., Chang, S.H.: Two dimensional carbon nanotube based strain sensor, *Sens. Actuators A Phys.*, **176**, 124 – 129, (2012).

19 Wang, M., Mu, L., Zhang, H., Ma, S., Liang, Y., Ren, L.: Flexible strain sensor with ridge-like microstructures for wearable applications, *Polym. Adv. Technol.*, **33**, 96 – 103, (2022).

20 Yao, Z., Feng, H., Shang, K., Deng, X., Yang, T.: Skin-like strain sensors based on multiwalled carbon nanotube/polydimethylsiloxane composite films, *ACS Appl. Nano Mater.*, **6**, 6550 – 6558, (2023).

21 Zhang, M., Yang, H., Li, H., Tong, L., Su, C., Feng, K., *et al.*: Transparent single crystal graphene flexible strain sensor with high sensitivity for wearable human motion monitoring, *J. Alloys Compd.*, **967**, 171724, (2023).

22 Zhang, W., Liu, Q., Chen, P.: Flexible strain sensor based on carbon black/silver nanoparticles composite for human motion detection, *Materials*, **11**, 1836, (2018).

23 Sankar, V., Nambi, A., Bhat, V.N., Sethy, D., Balasubramaniam, K., Das, S., *et al.*: Waterproof flexible polymer-functionalized graphene-based piezoresistive strain sensor for structural health monitoring and wearable devices, *ACS Omega*, **5**, 12682 – 12691, (2020).

24 Zhang, P., Tan, W.M., Tay, B.K.: Investigation of amorphous silicon-carbon films deposited by filtered vacuum cathodic arc, *J. Metastable Nanocryst. Mater.*, **23**, 351 – 354, (2005).

25 Yang, Y., Shen, H., Yang, Z., Yang, J., Wang, Z., Gao, K.: Highly flexible and sensitive wearable strain and pressure sensor based on porous graphene paper for human motion, *J. Mater. Sci. Mater. Electron.*, **33**, 17637 – 17648, (2022).

26 Ma, J., Qing, Y., Song, H., Yao, Y., Xu, X., Long, C., *et al.*: High-performance, superhydrophobic, and wearable strain sensor for amphibious human motion detection, *Adv. Mater. Technol.*, **8**, 2200798, (2023).

27 Njuguna, M.K., Yan, C., Hu, N., Bell, J.M., Yarlagadda, P.K.D.V.: Sandwiched carbon nanotube film as strain sensor, *Compos. Part B Eng.*, **43**, 2711 – 2717, (2012).

28 Rocha, J.G., Paleo, A.J., Van Hattum, F.W.J., Lanceros-Mendez, S.: Polypropylene-carbon nanofiber composites as strain-gauge sensor, *IEEE Sens. J.*, **13**, 2603 – 2609, (2013).

29 Lv, P., Yu, K., Tan, X., Zheng, R., Ni, Y., Wang, Z., *et al.*: Super-elastic graphene/carbon nanotube aerogels and their application as a strain-gauge sensor, *RSC Adv.*, **6**, 11256 – 11261, (2016).

30 Li, J., Xiang, D., Su, P., Zhao, C., Li, H., Li, Z., *et al.*: High-performance flexible strain sensors prepared by biaxially stretching conductive polymer composites with a double-layer structure, *Mater. Today Commun.*, **36**, 106548, (2023).

31 Zhou, Y., Zhan, P., Ren, M., Zheng, G., Dai, K., Mi, L., *et al.*: Significant stretchability enhancement of a crack-based strain sensor combined with high sensitivity and superior durability for motion monitoring, *ACS Appl. Mater. Interfaces*, **11**, 7405 – 7414, (2019).

32 Mahato, R., Masiul Islam, S.K., Maurya, R.K., Kumar, S., Purohit, G., Singh, S.: Flexible piezo-resistive strain sensors using all-polydimethylsiloxane based hybrid nanocomposites for wearable electronics, *Phys. Chem. Chem. Phys.*, **26**, 95 – 104, (2024).

33 Liu, D., Zhang, H., Chen, H., Lee, J.H., Guo, F., Shen, X., *et al.*: Wrinkled, cracked and bridged carbon networks for highly sensitive and stretchable strain sensors, *Compos. Part A Appl. Sci. Manuf.*, **163**, 107221, (2022).

34 Liu, Y., Yi, M., Chen, T., Mu, X., Sun, Q., Zhou, J.: Advances in graphene-based flexible wearable piezoresistive strain sensors, *J. Mater. Sci. Mater. Electron.*, **36**, 1211, (2025).

35 Yang, M., Liu, Y., Chen, H., Cai, J., Zhou, W.: Interwoven diamond grid-structured flexible strain sensor constructed with carbon nanotube-embedded PDMS, *Smart Mater. Struct.*, **35**, 015004, (2026).

36 Sindhu, B., Kothuru, A., Sahatiya, P., Goel, S., Nandi, S.: Laser-induced graphene printed wearable flexible antenna-based strain sensor for wireless human motion monitoring, *IEEE Trans. Electron Devices*, **68**, 3189 – 3194, (2021).